# Mode matching interface for efficient coupling of light into planar photonic crystals

Jeremy Witzens,* Michael Hochberg, Thomas Baehr-Jones, and Axel Scherer
*Department of Electrical Engineering 136-93, California Institute of Technology, Pasadena, California 91125, USA*
(Received 19 September 2003; revised manuscript received 25 November 2003; published 29 April 2004)

In order to integrate superdispersive elements based on photonic crystals, such as the superprism, with conventional integrated optics, insertion losses at the interface to the photonic crystal need to be reduced to an acceptable level. We describe a mode matching interface composed of cascaded diffraction gratings that generates the field profile of the photonic crystal Bloch mode from a slab mode. We calculate with three-dimensional finite-difference time-domain computation that by interposing such a multilayered grating between an unpatterned slab and a planar photonic crystal, the insertion efficiency is enhanced from 9% to 84%. Each diffraction grating consists of a row of holes and does not require any additional process steps from those used to fabricate the planar photonic crystal. In order to optimize the efficiency of the mode matching interface, constructive interference conditions are imposed between successive gratings and reflections from individual gratings are suppressed. We fabricate devices in silicon on insulator material and show experimental evidence of the Bloch mode structure and of the mode matching mechanism.

DOI: 10.1103/PhysRevE.69.046609 PACS number(s): 42.70.Qs, 42.82.Cr, 42.82.Gw

## I. INTRODUCTION

Anomalous dispersion properties of photonic crystals [1,2] such as ultrarefraction and negative refraction [3–6] have been intensely studied in the past years and have resulted in applications such as the superprism effect [7–9] and self-collimation [10–15]. In particular, the superprism effect has been singled out as a good candidate to develop a new generation of planar lightwave circuits for frequency domain demultiplexion. One of the crucial difficulties in using the superprism effect for practical planar demultiplexers is the coupling of light into the photonic crystal with acceptable insertion losses. Those insertion losses can be very high in the absence of mode matching because of the complex structure of the Bloch modes involved in the superprism effect. Although this is a crucial difficulty, it has received very limited attention in the previous literature. Baba and Ohsaki have proposed a mode matching interface and calculated its efficiency with 2D finite-difference time-domain computation (FDTD) [16]. Here we present a different approach that focuses on the problems related to the planar photonic crystal geometry, in particular, the out-of-plane scattering losses at the interface that can only be taken into account by 3D FDTD.

In the second section we analyze the structure of the Bloch modes involved in the superprism effect and derive the necessary functionality of the mode matching interface. The interface can then be designed and simulated independently of the planar photonic crystal (PPC). In order to provide physical intuition we derive the structure of the Bloch modes from general considerations such as the folding back of the dispersion diagrams into the first Brillouin zone (BZ) and the presence of cusps in the equifrequency contour. This also shows that the coupling difficulties outlined in this paper are intrinsic to the superprism effect and are not due to a particular geometry. We confirm those results by the numerical analysis of a Bloch mode chosen as an example. We introduce the multilayered grating (MLG) used to implement the mode matching interface (Sec. III), as well as the numerical methods used in this paper (the numerical data are generated by FDTD and then analyzed with the help of an inner product introduced in Sec. IV). The MLG is first optimized as a stand-alone device in Sec. V, and then integrated with the PPC in Sec. VI. This method considerably accelerates design iterations because the stand-alone MLG can be optimized with a transfer matrix method that is much faster than a full FDTD simulation. One of the conclusions of Sec. III is that cascading a higher number of diffraction gratings with a reduced scattering strength is beneficial because it reduces out-of-plane scattering losses and increases the mode overlap with the photonic crystal due to a finer adjustment of the MLG. However when a Gaussian beam is coupled into the PPC instead of a slab mode of infinite extent, additional difficulties arise and a more compact MLG with bigger holes and fewer cascaded gratings needs to be used (Sec. VII). Finally, we give experimental evidence of the Bloch mode structure by propagating light from a waveguide into a PPC and then into the unpatterned slab and by imaging the diffraction pattern of the electromagnetic field in the unpatterned slab (Sec. VIII). This experiment is repeated both with a bare PPC (without mode-matched interfaces) and with a mode-matched PPC.

Although the mode matching interface could easily be adapted to a triangular crystal lattice (the Bloch mode structure at the cusps of the equifrequency contours is essentially the same), we restrict ourselves to a square lattice PPC to compute quantitative results. A square lattice of holes (radius $r=0.15\ \mu$m) is etched into a silicon slab of thickness $t=205$ nm. The holes are backfilled with silicon dioxide and the slab is clad on both sides with silicon dioxide. The lattice constant is linked to the design of the MLG and varies slightly from case to case, but it is kept between 0.47 $\mu$m and 0.5 $\mu$m. In the calculations the refractive index of silicon is assumed to be 3.43 and the refractive index of silicon dioxide is assumed to be 1.46. The effective index of the slab

*Email address: witzens@caltech.edu

 

($n$) is equal to 2.77 at 1.52 $\mu$m. $\lambda$ is the free space wavelength.

## II. BLOCH MODE STRUCTURE

Due to the periodic nature of photonic crystals, photonic crystal modes (Bloch modes) can be described by functions of the following form (Bloch theorem):

$$f(\vec{r})e^{i\vec{k}\cdot\vec{r}}, \tag{1}$$

where $\vec{r}$ is the position vector, $\vec{k}$ is the reduced $k$ vector of the Bloch mode (in the first BZ) and $f$ is a function with the same periodicity as the photonic crystal. In the case of a PPC (2D periodicity) the Fourier transform of such a function takes the form

$$\sum_{a,b} f_{a,b}e^{i(\vec{k}+a\vec{K_1}+b\vec{K_2})\cdot\vec{r}}, \tag{2}$$

where $\vec{K}_1$ and $\vec{K}_2$ are the inverse lattice vectors of the PPC and $a$ and $b$ are integers. We call the lattice vectors of the PPC $\vec{e}_1$ and $\vec{e}_2$. $\vec{K}_1$ and $\vec{K}_2$ verify $\vec{K}_i\cdot\vec{e}_j=\delta_{ij}2\pi$. When more than one of the Fourier components in Eq. (2) carry a significant portion of the mode's power, there can be a significant mode mismatch between the Bloch mode of the PPC and an incoming slab mode, which corresponds to a single Fourier component.

The group velocity of light is given by $\vec{\nabla}_k(\omega)$, where $\omega$ is the angular frequency. This also holds for the group velocity of Bloch modes in photonic crystals, with the only difference that $k$ is the reduced $k$ vector [7]. $\vec{\nabla}_k(\omega)$ is normal to surfaces of constant $\omega$ (analogous to surfaces of constant energy in solid state physics, for example, the Fermi surface), or in the case of a PPC it is normal to contours of constant $\omega$. The equifrequency contour of an unpatterned slab is a circle centered on $\Gamma$ $(k=0)$, so that the group velocity of slab modes is collinear to the $k$ vector. However, in a photonic crystal equifrequency contours have features such as approximately flat sides and cusps (Fig. 1). This causes light to diffract in a PPC in a fundamentally different way than in an unpatterned slab. If the spread of $k$ vectors of a light beam corresponds to a flat side of the contour, the group velocities are collinear so that the beam stays collimated (self-collimation). On the contrary, in the region of the cusps the angular deflection in propagation direction corresponding to small changes in the $k$ vector is much higher than in the unpatterned slab (superprism effect).

The cusps in the equifrequency contour are due to coupling between two higher-order Fourier components. This coupling is induced by the periodic array of holes. On either side of the cusp, the Bloch mode is dominated by one of the Fourier components, while at the cusp itself the two components are of equal magnitude. In the case of the second band of a square lattice PPC, the equifrequency contours have a cusp on their intersection with the $\Gamma M$ direction, where $\Gamma$ and $M$ are the high-symmetry points shown in Fig. 1.

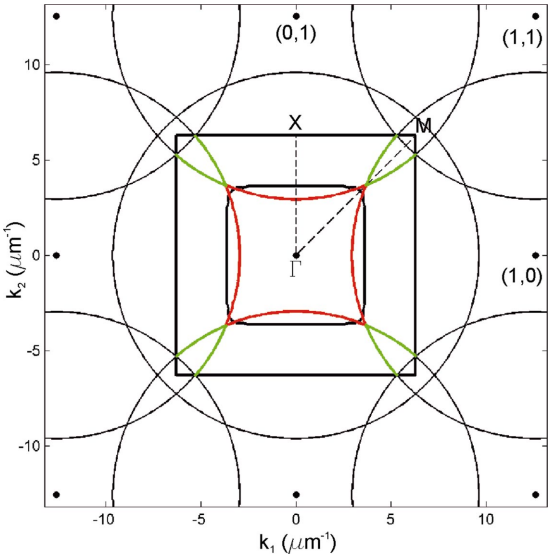


FIG. 1. (Color) This figure illustrates how the structure of the second band is formed by turning on coupling between higher-order Fourier components. The circle centered on $\Gamma$ is the equifrequency contour of an unpatterned slab of effective index $[(a^2-\pi r^2)n_{slab}+\pi r^2 n_{SiO_2}]/a^2$ ($\lambda=1.54$ $\mu$m), where $a$ is the lattice constant of the PPC (0.5 $\mu$m). The effective index is the weighted mean of the effective index of the unpatterned slab and of the refractive index of silicon dioxide (holes) so that we take into account the finite holes in the effective index but ignore the coupling and the anisotropy they induce. However, we represent by circles centered on $a\vec{K}_1+b\vec{K}_2$ the corresponding higher-order Fourier harmonics, where $a$ and $b$ are integers. The circles centered on (1,0) and (0,1) intersect inside the first BZ (represented by the black square) and anticross when coupling is turned on. The red contour represents the second band and the green contour the third band in the case of infinitesimal coupling. The real equifrequency contour of the second band is also represented (black squarish contour). Even though the structure is more complex in the case of finite coupling, the mode on the intersection between the equifrequency contour of the second band and the $\Gamma M$ direction is essentially composed of two Fourier components offset by $\vec{K}_1$ and $\vec{K}_2$ from the first BZ. The exact Fourier structure of such a mode is represented in Fig. 2. The axes of the figure show $k_1=\vec{k}\cdot\vec{e}_1$ and $k_2=\vec{k}\cdot\vec{e}_2$.

Before we give a numerical analysis of the Bloch modes of the square lattice PPC, we derive the Bloch mode structure at the cusp from more general considerations, so as to relate it to the presence of the cusp rather than to a particularity of the square lattice. As a thought experiment, we start with a homogeneous medium and progressively turn on coupling between higher-order spatial Fourier components. This gives an adequate description of the band structure in the limit of very small hole size. In the case of finite hole size the equifrequency contours as well as the Bloch mode structure are modified, however, the essential characteristics are the same and can be intuitively understood with the weak coupling model.

In Fig. 1 we represent the equifrequency contour of an unpatterned slab of effective index $[(a^2-\pi r^2)n_{slab}+\pi r^2 n_{SiO_2})]/a^2$ for $\lambda=1.54$ $\mu$m (circle centered on $\Gamma$).

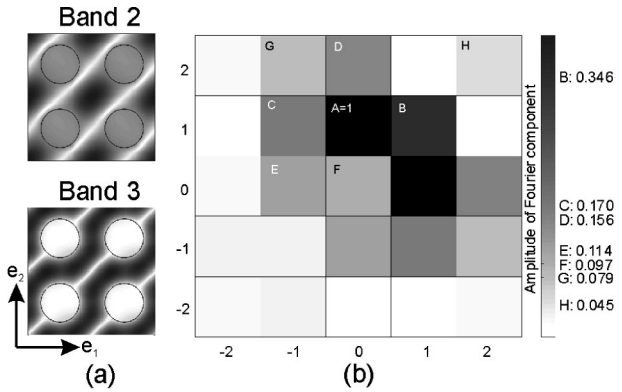


FIG. 2. (a) Field profiles (amplitude of the out of plane component of the $B$ field, $B_3$, on the center plane of the PPC) of modes of the second and third bands located on $\Gamma M$ (at $\lambda = 1.55\ \mu$m). The mode of the second band has a field maximum in the high index region at the center of the figure, where the mode of the third band has a field minimum. (b) Fourier structure of the mode of the second band obtained by taking the Fourier transform of $B_3$. The amplitudes of the Fourier components are shown. The axis gives the offset of the Fourier components from the component in the first BZ in integer multiples of $\vec{K}_1$ and $\vec{K}_2$.

The lattice constant $a$ of the PPC equals 0.5 $\mu$m and the effective index is the weighted mean of the effective index of the unpatterned slab and of the refractive index of silicon dioxide (holes). This corresponds to a medium with the same ratio of high index regions (slab) and low index regions (holes), but where the anisotropy and the coupling induced by the holes is ignored. We also represent the higher-order Fourier harmonics created by the lattice (circles centered on $a\vec{K}_1 + b\vec{K}_2$, where $a$ and $b$ are integers). The (1,0) harmonic and the (0,1) harmonic intersect inside the first BZ on $\Gamma M$. When the coupling between the Fourier components is ''turned on'' (small but nonvanishing hole size) the two Fourier components anticross and two disjoint contours are formed. The resulting contours correspond to the second band (red) and to the third band (green) of the photonic crystal. The fourth band corresponds to the (1,1) harmonic (it also intersects $\Gamma M$ inside the first BZ). On $\Gamma M$, the Bloch modes of the second and third bands are essentially composed of two Fourier harmonics respectively, offset from the first BZ by $\vec{K}_1$ and by $\vec{K}_2$, while the Bloch modes of the fourth band are essentially composed of a single Fourier component.

In the case of a finite hole size there will also be other Fourier components in the Bloch mode structure and the equifrequency contour has a slightly different shape (compare the true equifrequency contour in Fig. 1 to the red contour that corresponds to the limit of vanishing coupling), but the Bloch mode is still dominated by the same two higher-order components. As an example, we operated a Fourier decomposition on one particular Bloch mode of the PPC (second band on $\Gamma M$ at $\lambda = 1.55\ \mu$m). Figure 2 shows the detailed Fourier structure of the mode. The power shared between the two main components is calculated to be 87%. We conclude that in order to couple into these Bloch modes the two dominant higher-order Fourier components need to be generated from the incoming slab mode.

The $\Gamma M$ direction corresponds to $\vec{e}_1 + \vec{e}_2$ in real space. The interface between the PPC and the slab is chosen to be along $\vec{e}_1 - \vec{e}_2$ so that a slab mode with a propagation direction perpendicular to the interface is coupled to a Bloch mode on the $\Gamma M$ direction, on the cusp of the equifrequency contour.

When a Bloch mode crosses the interface from the PPC to the unpatterned slab it generates higher diffraction orders in the unpatterned slab. Conversely, in order to insert a slab mode (single Fourier component) into the PPC, those higher-order Fourier components need to be generated from the slab mode by the mode matching interface. In order to design the mode matching interface, the relative strength and phase of those diffraction orders needs to be evaluated from the Fourier structure of the Bloch mode. Thus we need to establish a correspondence between the Fourier components of the Bloch mode and the diffraction orders in the slab. We denote by $\vec{n}_\perp$ the normalized vector along the interface, $(\vec{e}_1 - \vec{e}_2)/\|\vec{e}_1 - \vec{e}_2\|$. The projection of the $k$ vector of the Fourier components onto the interface, $k_\perp = \vec{k} \cdot \vec{n}_\perp$, indicates the diffraction orders to which the Fourier components contribute. The Fourier component (1,1) corresponds to the zeroth diffraction order, $k_\perp = \vec{k} \cdot \vec{n}_\perp = 0$. The two dominant components (1,0) and (0,1) project to $k_\perp = (\vec{k} + \vec{K}_{1/2}) \cdot \vec{n}_\perp = \pm 2\pi/A$ and contribute to higher diffraction orders, where $A = \sqrt{2}a$ is the periodicity of the holes at the interface and $a$ is the lattice constant of the PPC. The correspondence between the Fourier components in the Bloch mode structure and the amplitude of their contribution to the corresponding diffraction orders is not exactly one to one, however we can conclude that the 1 and $-1$ diffraction orders ($k_\perp = \pm 2\pi/A$) are dominant.

Furthermore, we can classify Bloch modes on the $\Gamma M$ direction by their symmetry relative to $\Gamma M$ (in real space the surface generated by $\vec{e}_1 + \vec{e}_2$ and $\vec{e}_3 = \vec{e}_1 \wedge \vec{e}_2$). More precisely we consider the symmetry operator $S$ defined by a surface generated by $\vec{e}_1 + \vec{e}_2$ and $\vec{e}_3$ and passing through the center of a hole. Then $\sigma_S = -1$ for the second band (even $B$ field and odd $E$ field) and $\sigma_S = 1$ for the third band (odd $B$ field and even $E$ field). We consider quasi-TE modes so that the field intensity on the center plane of the slab is best described by $B_3 = \vec{B} \cdot \vec{e}_3$. There is a high index region on the symmetry plane $S$ (at the center of the square defined by four adjacent holes, Fig. 2). For the second band, $B_3$ has a maximum in that region, while for the third band $B_3$ is antisymmetric and has an antinode on $S$. The different field overlaps with the low and the high index regions create the wide splitting between those two bands. For more details on symmetries in photonic crystals see Ref. [17].

## III. MULTILAYERED GRATING

A grating formed by a row of holes of pitch $A$, parallel to the edge of the PPC, diffracts an incoming plane wave to higher diffraction orders offset by $K_{grating} = \pm 2\pi/A$ and is as such suitable to generate the higher-order harmonics com-

prising the Bloch mode. However, the diffraction efficiency of a single grating is insufficient (for example, 15% diffraction efficiency was computed by FDTD for holes of radius $r=0.15\ \mu$m). Hence several gratings are cascaded. To improve efficiency, constructive interference conditions are imposed between the contributions of the successive gratings to the higher diffraction orders and destructive interference conditions are imposed between the reflections generated by the successive gratings (antireflection conditions). We will show that those interference conditions can be reduced to two independent equations and that it is possible to satisfy both conditions at the same time for certain values of the PPC lattice constant. In the following ''coupling efficiency'' characterizes the stand-alone MLG and corresponds to the power transfer from the zeroth order into the first order. On the other hand, insertion efficiency, characterizes the MLG integrated with the PPC and corresponds to the insertion efficiency into the PPC.

For the range of lattice constants used in this paper the only diffraction orders that are supported by the slab are $-1$, 0, and 1 ($|2\pi m/A|<2\pi n/\lambda$ where $m$ is the order of the diffraction order). The correct field symmetry to couple into the second band is obtained when the holes of the gratings are in front of the holes of the PPC, or when the holes of the gratings are offset by $A/2$. This can be seen by the fact that the incoming TE slab mode has the correct symmetry and that the symmetry along $S$ is preserved by the gratings in those two cases. If the offset is different from 0 or $A/2$ (modulo $A$), the symmetry is broken. In the following the holes of the grating will be offset by $A/2$ (Fig. 5). The 1 and $-1$ diffraction orders have the same magnitude and have the same phase (defined as the phase of $B_3$ on $S$) so that they can be described by a single scalar, referred to as order 1 in the following. The characteristic of the grating then reduces to scattering between four slab modes of identical symmetry relative to $S$ (order 0, order 1, and their counterpropagating counterparts) and scattering to free space modes (out-of-plane scattering losses). Hence, the grating can be described by a $4\times4$ lossy scattering matrix.

We call $\theta$ the diffraction angle ($\theta=\sin^{-1}[2\pi/(Ak)]$), $\varphi_0=\varphi_{0\to0}$ the phase accumulated by the zeroth order after transmission through a single grating, $\varphi_1=\varphi_{1\to1}$ the phase accumulated by the first order, and $\varphi_{0\to1}$ the phase acquired by the fraction of the zeroth order scattered into the first order by a single grating ($\varphi_0$, $\varphi_1$, and $\varphi_{0\to1}$ are the phases of elements of the scattering matrix of a single grating). $\lambda_0$ is the target wavelength, $d$ is the spacing between successive gratings, and $n$ is the effective index of the slab. The constructive interference condition between the two forward propagating modes (order 0 and order 1) is obtained when

$$\varphi_0+dn\frac{2\pi}{\lambda_0}=\varphi_1+\cos(\theta)dn\frac{2\pi}{\lambda_0}+2\pi m_1, \tag{3}$$

where $m_1$ is an integer. The antireflection conditions, respectively for reflections from the zeroth order to the zeroth order [Eq. (4)], from the first order to the first order [Eq. (5)], and from the zeroth order to the first order [Eq. (6)] are given by

$$2\varphi_0+2dn\frac{2\pi}{\lambda_0}=\pi+2\pi m_2 \tag{4}$$

$$2\varphi_1+2\cos(\theta)dn\frac{2\pi}{\lambda_0}=\pi+2\pi m_3, \tag{5}$$

$$\varphi_0+\varphi_1+dn\frac{2\pi}{\lambda_0}[1+\cos(\theta)]=\pi+2\pi m_4, \tag{6}$$

where $m_{2,3,4}$ are integers. Equation (6) is also the antireflection condition for reflections from the first order to the zeroth order. Equation (3) implies that Eqs. (4)–(6) are equivalent with $m_3=m_2-2m_1$ and $m_4=m_2-m_1$, so that only Eqs. (3) and (4) need to be satisfied to suppress all reflections. Since $d$, $\theta$, and $a$ are functions of $m_1$, $m_2$, and $\lambda_0$, the lattice constant of the PPC is linked to the design of the MLG.

Equations (4)–(6) ensure that zero reflection is achievable in the limit of small MLG holes. The small holes are necessary because otherwise the reflection of the first grating cannot be compensated. This is the same phenomenon as the reflections from a distributed Bragg reflector (DBR) at the antireflection condition, i.e., if the scattering efficiency of a single grate is too high, the reflections due to the first grate can not be compensated [18,19]. When the reflections vanish, the two forward traveling diffraction orders can be modeled as coupled forward traveling waves. Thus they can be modeled by an effective two by two transfer matrix in the limit of small holes. The device behaves like a directional coupler with a coupling length that can only take a set of discrete values whose step is dependant on the hole size. In the limit of vanishing hole size the effective coupling length behaves like a continuous parameter. Equation (3) implies that the elements on the diagonal of the effective 2 by 2 transfer matrix have the same phase (i.e., the zeroth diffraction order and the first diffraction order accumulate the same phase while propagating forward). $(2\varphi_{0\to1}-\varphi_0-\varphi_1)/2$ is the phase difference between the coupling coefficient in the 2 by 2 transfer matrix and the diagonal terms.

There is one last condition that is necessary to achieve 100% extinction of the zeroth order (i.e., a coupling efficiency of the MLG uniquely limited by out-of-plane scattering losses). If $(2\varphi_{0\to1}-\varphi_0-\varphi_1)/2=\pm\pi/2$ the MLG behaves like a symmetric directional coupler and 100% power transfer is possible if the adequate coupling length is chosen (power coupled from the zeroth order into the first order and then back into the zeroth order interferes destructively with the field that stayed in the zeroth order). If $(2\varphi_{0\to1}-\varphi_0-\varphi_1)/2\neq\pm\pi/2$ the maximum power transfer is less than 100%. It can be derived from first principles (power conservation and reciprocity imposed on the scattering matrix) that in the limit where individual holes constituting the grating have small coupling efficiency (small radius) this phase tends to $-\pi/2$. In that limit $\varphi_0\to0$ and $\varphi_1\to0$ (if the scattering efficiency of the holes is vanishing a slab mode is transmitted unperturbed through the grating and does not accumulate an extra phase). It can then be derived from power conservation (unitarity of the transfer matrix) and from reciprocity that $\varphi_{0\to1}\to\pm\pi/2$.

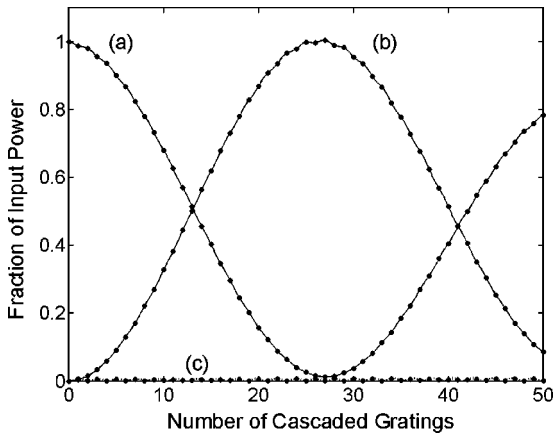


FIG. 3. Transmission (a), coupling efficiency (b), and reflection (c) of the multilayered grating (hole size 40 nm) as computed by the transfer matrix method for $\lambda = 1.52\ \mu$m. The coupling efficiency is defined as the power transferred from the zeroth order into the first order, the transmission as the power remaining in the first order. Optimum coupling is obtained with 27 layers.

The coupling efficiency is still limited by scattering losses. With numerical examples we will show that a structure with more layers of smaller holes has less scattering losses than a structure with fewer gratings of larger holes. The MLG described in Sec. V (Fig. 3) is composed of 40 nm holes while the MLG described in Sec. VII (Fig. 10) is composed of 0.15 $\mu$m holes. With the bigger holes the maximum coupling efficiency is 70% and is limited by out-of-plane scattering losses.

In short, we showed that if the MLG is designed with small holes, reflections are suppressed and out-of-plane scattering losses reduced, and that the coupling efficiency of the MLG can be chosen between 0 and near 100% on a quasicontinuous scale. In Sec. V we will implement a MLG with a hole size of 40 nm that verifies this.

## IV. INNER PRODUCT

The analyses conducted in the next sections are based to a large extent on the decomposition of the electromagnetic field into modes of the unpatterned slab. This decomposition is performed with an inner product introduced in this section.

For waveguides with continuous translation symmetry, orthogonality conditions are well established [20], in particular, for a nonabsorbing waveguide with translation symmetry in the $z$ direction, and two modes (bound or radiative) $\psi = (\mathbf{E},\mathbf{H})$ and $(\overline{\psi} = \overline{\mathbf{E}},\overline{\mathbf{H}})$ with the same implicit time dependence $\exp(-i\omega t)$

$$\mathbf{E} = \mathbf{e}(x,y)e^{i\beta z}, \quad \mathbf{H} = \mathbf{h}(x,y)e^{i\beta z} \tag{7}$$

$$\overline{\mathbf{E}} = \overline{\mathbf{e}}(x,y)e^{i\overline{\beta} z}, \quad \overline{\mathbf{H}} = \overline{\mathbf{h}}(x,y)e^{i\overline{\beta} z} \tag{8}$$

where $\omega$ is the angular frequency and $\beta$ and $\overline{\beta}$ are the propagation constants. If $\beta - \overline{\beta} \neq 0$, the following holds for a surface $A$ normal to $\hat{z}$.

$$\int_A \{\mathbf{e} \times \overline{\mathbf{h}^*} + \overline{\mathbf{e}^*} \times \mathbf{h}\} \cdot \hat{\mathbf{z}} dA = 0. \tag{9}$$

This functional is taken as the inner product. It has previously been applied to photonic crystal modes [21].

$|\phi\rangle$ is a given field profile to be analyzed (field cross section perpendicular to $\vec{e}_1 + \vec{e}_2$) and $|\psi\rangle$ a normalized mode profile (normalized to 1 if it is forward propagating and to $-1$ if it is backward propagating). Then

$$P = \langle \phi | \phi \rangle, \tag{10}$$

$$P_\psi = \langle \psi | \phi \rangle^2 \mathrm{sgn}(\langle \psi | \psi \rangle), \tag{11}$$

where $P$ is the power carried by $|\phi\rangle$ and $P_\psi$ the power carried by the projection of $|\phi\rangle$ onto $|\psi\rangle$. Note that $P = \Sigma_i \langle \psi_i | \phi \rangle^2 \mathrm{sgn}(\langle \psi_i | \psi_i \rangle)$, where the sum is taken over all the modes of the system, but because the inner product is not positive definite $P \leqslant \Sigma_i |\langle \psi_i | \phi \rangle|^2$.

The Bloch mode is decomposed into forward propagating modes of the unpatterned slab ($|\phi\rangle_{FP}$) and backward propagating modes of the unpatterned slab ($|\phi\rangle_{BP}$). Those components correspond to the projection of the Bloch modes onto the modes of the unpatterned slab [Eqs. (12) and (13)]. The slab is single mode, so that the TE modes of the slab can be unambiguously referred to by the angle between $\vec{e}_1 + \vec{e}_2$ and their direction of propagation. Furthermore, only slab modes with propagation directions corresponding to $\theta$, 0°, and $-\theta$ as well as their counterpropagating counterparts have a finite overlap with the Bloch mode and its diffraction pattern. The forward propagating modes are $|\psi_{-\theta}\rangle$, $|\psi_{0°}\rangle$, and $|\psi_\theta\rangle$, the backward propagating modes are $|\psi_{180°-\theta}\rangle$, $|\psi_{180°}\rangle$, and $|\psi_{180°+\theta}\rangle$. We couple to Bloch modes with a given symmetry ($\sigma_S = -1$), so that we only need to take into account $|\psi_1\rangle = 1/\sqrt{2}(|\psi_{-\theta}\rangle + |\psi_\theta\rangle)$, $|\psi_0\rangle = |\psi_{0°}\rangle$, $|\overline{\psi}_1\rangle = 1/\sqrt{2}(|\psi_{180°-\theta}\rangle + |\psi_{180°+\theta}\rangle)$, and $|\overline{\psi}_0\rangle = |\psi_{180°}\rangle$, where the relative phase between modes in the sums is chosen so as to satisfy $\sigma_S = -1$. $|\psi_0\rangle$ and $|\psi_1\rangle$ correspond to the zeroth and first diffraction orders.

$$|\phi\rangle_{FP} = \langle \psi_0 | \phi \rangle |\psi_0\rangle + \langle \psi_1 | \phi \rangle |\psi_1\rangle, \tag{12}$$

$$|\phi\rangle_{BP} = -\langle \overline{\psi}_0 | \phi \rangle |\overline{\psi}_0\rangle - \langle \overline{\psi}_1 | \phi \rangle |\overline{\psi}_1\rangle. \tag{13}$$

The minus signs in Eq. (13) are due to the fact that the backwards propagating modes are normalized to $-1$.

## V. CHARACTERIZATION OF THE STAND-ALONE MULTILAYERED GRATING

We design a MLG with holes of radius 40 nm and with design parameters $\lambda_0 = 1.52\ \mu$m, $m_1 = 1$, and $m_2 = 4$, which results in $a = 0.470\ \mu$m and $d = 1.240\ \mu$m.

The transfer matrix characterizing a single row of holes is computed by using FDTD with a spatial discretization of 20 nm and a time step of $0.011\,43\ \mu\mathrm{m}^{-1}$ in units of $c_0 = 1$ (where $c_0$ is the speed of light in vacuum). A silicon slab with a single hole ($r = 40$ nm) is placed in a computational domain of dimensions $A \times 1.2\ \mu\mathrm{m} \times 100\ \mu$m (respectively,

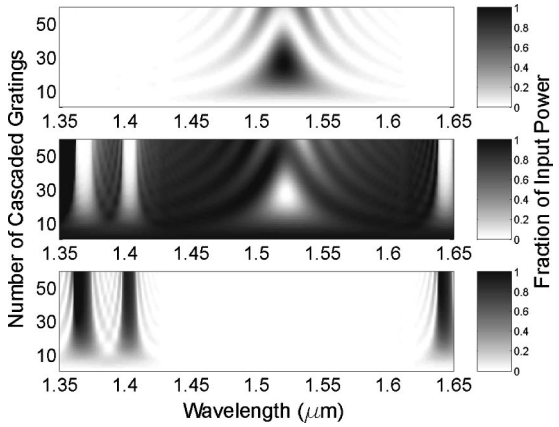


FIG. 4. Coupling efficiency (upper plot), transmission (middle plot), and reflection (lower plot) of the MLG as a function of wavelength and of the number of cascaded gratings. The optimum coupling efficiency is obtained at $\lambda = 1.52$ $\mu$m and 27 layers; however, the passband of the MLG is higher for a smaller number of cascaded gratings.

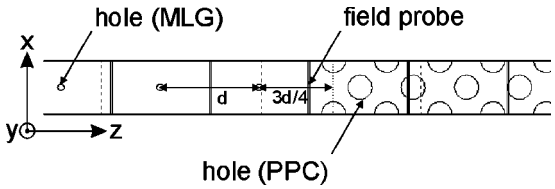


FIG. 5. Configuration of the simulation. The width ($x$ direction) is $A$ so that a single hole per cascaded grating is placed in the computational domain. Bloch boundary conditions are applied ($x$ direction) so as to effectively simulate an infinite grating and an infinite PPC in the $x$ direction. The field is launched in the unpatterned slab, propagates through the MLG, and is transmitted into the PPC. Field probes are periodically placed with a separation $d$ between them, first inside the MLG at equal distance from adjacent gratings and then inside the PPC. The distance between the MLG and the PPC is chosen so as to impose the correct phase relationship between the zeroth and the first order for optimum insertion into the Bloch mode. This results in the distance $3d/4$ between the last grating of the MLG and the first row of the PPC (hole center to hole center).

$x$, $y$, and $z$, where $x$ is along the interface $\vec{e}_1 - \vec{e}_2$, $y$ is along the out-of-plane direction $\vec{e}_3$, and $z$ is along the direction of propagation $\vec{e}_1 + \vec{e}_2$). Bloch boundary conditions (BBC) with a zero phase are applied in the $x$ direction so as to effectively simulate an infinite grating. Absorbing boundary conditions (ABC) are applied in the other directions. The zero phase is compatible with $|\psi_0\rangle$ ($k_x = k_\perp = 0$) and with the higher diffraction order $|\psi_1\rangle$ ($k_\perp = \pm 2\pi/A$ so that $k_\perp = 0$ modulo $2\pi/A$).

Successively $|\psi_0\rangle$ and $|\psi_1\rangle$ are launched and propagated through the hole. Probes store field profiles before and after the hole. By taking the inner product with $|\psi_0\rangle$, $|\psi_1\rangle$, $|\overline{\psi}_0\rangle$, and $|\overline{\psi}_1\rangle$ all the coefficients of the scattering matrix are extracted. The transfer matrix is then computed from the scattering matrix. By exponentiating the transfer matrix and imposing as a boundary condition only forward propagating waves at the output boundary of the MLG, the properties of MLG with a variable number of cascaded layers are computed.

Figure 3 shows the transmission (zeroth order to zeroth order), coupling (zeroth order to first order), and reflections of the MLG as a function of the number of cascaded gratings at $\lambda = 1.52$ $\mu$m, as computed by the transfer matrix method. It is apparent that the optimum coupling efficiency is reached with 27 layers. FDTD simulations of the full MLG are in good agreement with the transfer matrix method (at $\lambda = 1.51$ $\mu$m, the optimum is computed to be 26 layers with the transfer matrix method and to be 23 layers with a full FDTD simulation). Figure 4 shows the results of the transfer matrix method as a function of both the number of cascaded gratings and of the wavelength. The triangular shape of the transmission shows that there is an inherent trade-off between the maximum coupling efficiency and the pass band (the maximum coupling efficiency is achieved with 27 layers; however, the pass band is higher for a smaller number of layers). This will be reflected in the insertion efficiency and pass band of the mode-matched photonic crystal as shown in Sec. VI (Fig. 9).

## VI. INTEGRATION OF THE MULTILAYERED GRATING WITH THE PLANAR PHOTONIC CRYSTAL

The relative phase between $|\psi_0\rangle$ and $|\psi_1\rangle$ can be adjusted by choosing the distance $d_{MLG \to PPC}$ between the last row of the MLG and the first row of the PPC (Fig. 5). Inside the PPC, $|\psi_0\rangle$ and $|\psi_1\rangle$ are in phase in the high index region between four adjacent holes [Fig. 2(a)]. This also holds for the first row of the PPC and constrains $d_{MLG \to PPC}$. For $m_1 = 1$ and $\varphi_{0\to 1} - \varphi_0 = -\pi/2$, this results in $d_{MLG \to PPC} = 3d/4$. Indeed the distance $3d/4$ introduces a phase shift $\varphi_{|\psi_1\rangle} - \varphi_{|\psi_0\rangle} = -3/4 m_1 2\pi = -3\pi/2$. At the last row of the MLG $\varphi_{|\psi_1\rangle} - \varphi_{|\psi_0\rangle} = \varphi_{0\to 1} - \varphi_0 = -\pi/2$ so that the resulting phase difference at the first row of the PPC is $-3\pi/2 - \pi/2 = -2\pi$.

As for the calculation of the transfer matrix we apply BBC in the $x$ direction to a computational domain of dimensions $A \times 1.2$ $\mu$m $\times 100$ $\mu$m. The slab mode $|\psi_0\rangle$ is launched at the beginning of the MLG. After 40 000 time steps the wave packet traveling in the PPC reaches the ABC at $+z$ [Fig. 6(a)]. Between subsequent layers of the MLG, as well as inside the PPC, probes store the field profile ($|\phi\rangle$). We stop all simulations after 50 000 time steps so that the reflection of the Bloch mode at the $+z$ interface does not reach the field probes and bias the data. The inner product is taken between the field profiles and $|\psi_0\rangle$, $|\psi_1\rangle$, $|\overline{\psi}_0\rangle$, and $|\overline{\psi}_1\rangle$ (see Figs. 6 and 7). Note that the inner product is defined between field cross sections of same implicit time dependence, so that a temporal Fourier transform needs to be applied to the time series before the inner product.

We compute throughout the MLG and the PPC the power carried by (i) the order 0 ($|\langle \psi_0 | \phi \rangle|^2$), (ii) the order 1 ($|\langle \psi_1 | \phi \rangle|^2$), (iii) the total power carried by forward propagating slab modes (i.e., the sum of the previous two), and

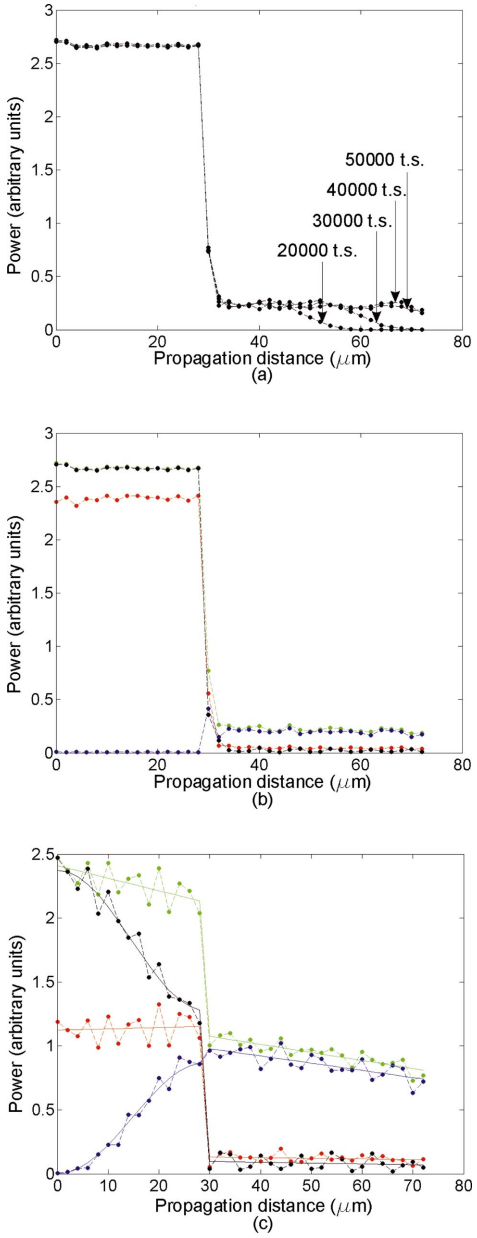


FIG. 6. (Color) Field decomposition obtained from the field probes. (a) and (b) correspond to a non-mode-matched PPC ($\lambda = 1.51$ $\mu$m) and (c) corresponds to a PPC integrated with an MLG of 14 layers that operates partial mode matching [$\lambda = 1.49$ $\mu$m, compare with Fig. 7(a)]. In (a) $|\langle\psi_0|\phi\rangle|^2+|\langle\psi_1|\phi\rangle|^2$ is shown for various time steps after the start of the FDTD simulation. In (b) and in (c) the black curve shows $|\langle\psi_0|\phi\rangle|^2$ [(i) in the text)], the blue curve shows $|\langle\psi_1|\phi\rangle|^2$ (ii), the green curve shows $|\langle\bar{\psi}_0|\phi\rangle|^2 + |\langle\psi_1|\phi\rangle|^2$ (iii), and the red curve shows $|\langle\bar{\psi}_0|\phi\rangle|^2+|\langle\bar{\psi}_1|\phi\rangle|^2$ (iv). It is apparent in (b) that the zeroth order is reflected (black line) and that the first order is transmitted (blue line).

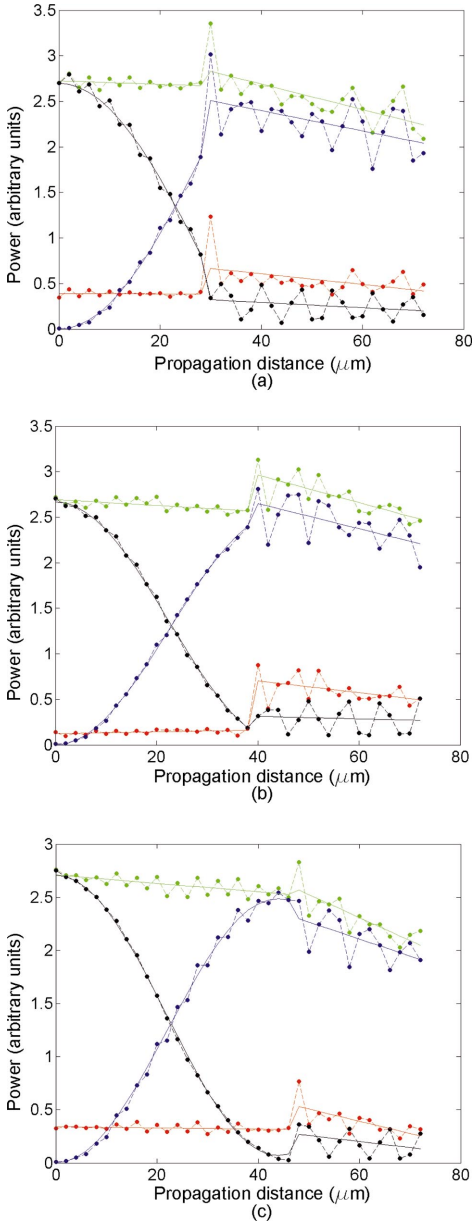


FIG. 7. (Color) Field decomposition obtained from the field probes for a PPC integrated with an MLG with (a) 14 layers, (b) 19 layers and (c) 23 layers ($\lambda = 1.51$ $\mu$m in all three cases). The MLG in (a) has less then the optimum number of layers (not enough power coupled into the first order), (b) corresponds to the optimum number of layers and the MLG in (c) has too many layers. In (c) the coupling from the zeroth order into the first order is maximized, however, the insertion efficiency into the PPC is suboptimum because the Bloch mode has a small fraction of its power in the zeroth order. The color conventions are the same as in Fig. 6.

(iv) the total power carried by backward propagating slab modes ($|\langle\bar{\psi}_0|\phi\rangle|^2+|\langle\bar{\psi}_1|\phi\rangle|^2$). We evaluate the insertion efficiency by

$$\frac{P_{fwd,PPC}-P_{bwd,PPC}}{P_0}, \tag{14}$$

where $P_{fwd,PPC}$ is the power carried by forward propagating slab modes (iii) at the first probe after the interface, $P_{bwd,PPC}$ is the absolute value of the power carried by backward propagating modes (iv) at that same probe and $P_0$ is the power carried by forward propagating modes (iii) before the MLG (i.e., the power that was initially launched). Forward propagating Bloch modes in a PPC have components that would correspond to backward propagating modes in the

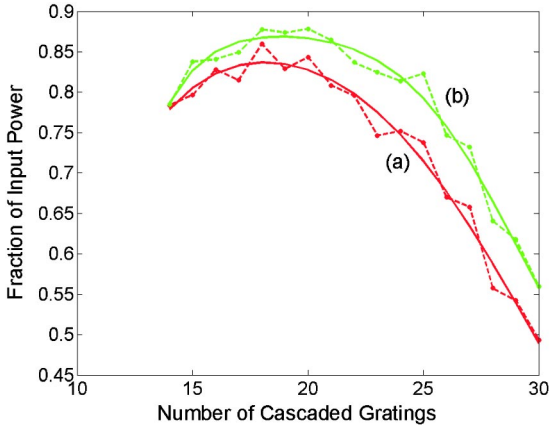


FIG. 8. (a) Insertion efficiency as a function of the number of cascaded gratings in the MLG for $\lambda = 1.51$ $\mu$m and (b) fraction of the output power of the MLG transmitted into the PPC. (b) normalizes out the losses due to out-of-plane scattering inside the MLG, in order to evaluate the insertion losses uniquely due to mode mismatch.

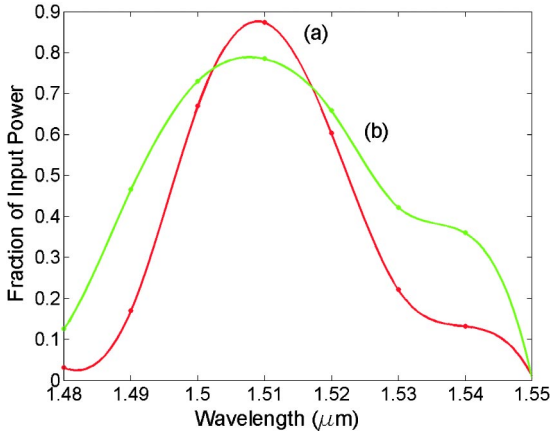


FIG. 9. Insertion efficiency as a function of frequency for (a) 19 layers and (b) 14 layers. Optimum insertion efficiency is achieved in the case of 19 layers at 1.51 $\mu$m (84%), however, the bandpass is higher in the case of 14 layers (45 nm vs 28.5 nm).

slab so that $P_{bwd,PPC}$ has to be taken into account in Eq. (14).

Figure 6 shows (i), (ii), (iii), and (iv) as a function of the propagation distance ($z$) for a bare PPC and for a PPC integrated with a MLG that operates partial mode matching. In Fig. 6(b) the PPC is not mode matched and almost all the power is reflected (9% insertion efficiency). In Fig. 6(c) the MLG operates partial mode matching. At the interface, the power remaining in the zeroth order is almost completely reflected, while the power in the first order is transmitted into the photonic crystal. However, this picture can be refined. The Bloch modes have most of their power in the higher diffraction order, but there is still a finite amount of power in the zeroth order. Thus the optimum insertion efficiency is not at 100% coupling efficiency (of the MLG) but at a slightly lower coupling efficiency. This is illustrated by Fig. 7. In (a) the coupling into the first order is insufficient and there is a sharp drop at the interface in the power carried by the zeroth order. In (c) the MLG has near 100% power transfer into the first order but the situation is still suboptimal because there is not enough power in the zeroth order. The power in the zeroth order increases at the interface, the power in the first order decreases, and the ratio between the two components is changed inside the PPC. There are additional reflections as compared to (b). The situation is optimum in (b) and the reflection is minimum. Note that both the power in the first order and in the zeroth order increase at the interface. This does not contradict power conservation because the power carried in back propagating slab modes also increases at the interface.

For $\lambda = 1.51$ $\mu$m, we plotted the insertion efficiency as a function of the number of gratings composing the MLG (Fig. 8), i.e., the power transmitted into the PPC normalized by the power initially launched into $|\psi_0\rangle$. We also plotted the power transmitted into the PPC normalized by the power contained in forward traveling modes (iii) after the MLG and before the PPC. This normalizes out the losses incurred inside the MLG due to out-of-plane scattering and is a better characterization of the mode mismatch. It is apparent that mode mismatch is the main limiting factor (the maximum power transmission is 83.7%, versus 86.9% without out-of-plane scattering losses).

There are some fundamental limits to this coupling scheme that may explain the remaining insertion losses. Only the components of the Bloch mode that correspond to forward propagating modes of the slab ($|\psi_0\rangle$ and $|\psi_1\rangle$) are generated. However the Bloch mode also contains components that would be back-propagating in the slab, such as component $E$ in Fig. 2. There are also components orthogonal to the radiative modes of the slab, for example, higher-order Fourier components with $k_x > 2\pi n/\lambda$ that cannot propagate in the unpatterned slab (for example, components $C$ and $D$ in Fig. 2).

In Fig. 9 we show the insertion efficiency as a function of wavelength. As predicted, there is a trade-off between the best peak efficiency (19 layer MLG) and the pass band. For a 19 layer MLG the peak efficiency is 84% (as compared to 9% without mode matching interface) and the full width at half maximum (FWHM) is 28.5 nm. For a 14 layer MLG the peak efficiency is 79% and the FWHM is 45 nm.

## VII. COMPACT DESIGN FOR GAUSSIAN BEAMS

In Sec. III we have shown that if a slab mode of infinite extent is coupled into the PPC, a MLG composed of many layers of small holes is more efficient than a MLG with fewer cascaded gratings and larger holes. Reflections are suppressed, maximum achievable coupling efficiency is higher, and out-of-plane scattering losses decrease. However, when a beam of finite width (e.g. a Gaussian beam) is coupled into the PPC, the higher diffraction orders generated inside the MLG propagate in different directions than the zeroth order, so that the three beams separate. The MLG will only function as an efficient coupling scheme if the initial beam is much wider than the depth of the MLG (number of cascaded gratings times $d$). Then the beam separation will only be a fringe effect.

We design a MLG with a hole size $r = 0.15$ $\mu$m and with

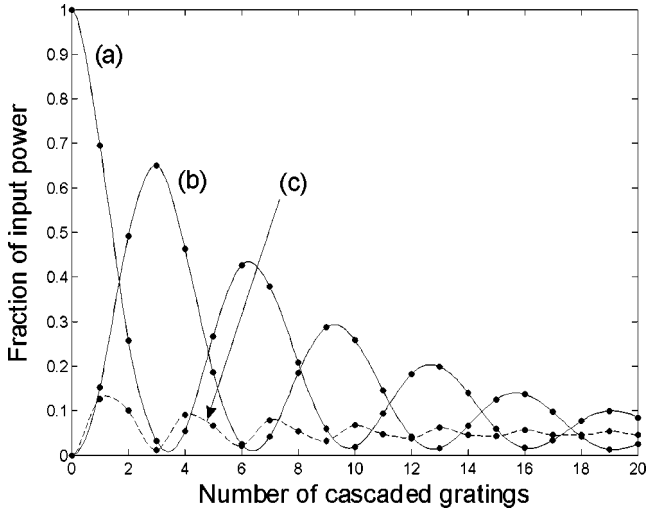


FIG. 10. Transmission (a), coupling efficiency (b), and reflection (c) of the multilayered gratings at the target wavelength $\lambda = 1.52\ \mu$m for a hole radius of 0.15 $\mu$m. The optimum coupling efficiency is achieved with three cascaded gratings. The coupling efficiency is limited by out-of-plane scattering losses. It can be seen that transmission and reflection of the three layer MLG are close to zero and are not limiting the coupling efficiency in a significant way.

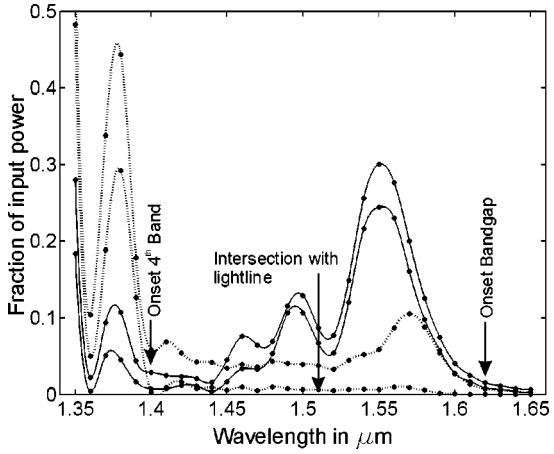


FIG. 11. Transmission through the stand-alone PPC (dashed) and through the mode-matched PPC (continuous). In both cases the upper curve is the total power transmission and the lower curve the power transmitted into the zeroth order. Points show computed data points. The oscillations in the transmission might be due to a Fabry-Perot resonance between the edges of the PPC. The third band has an antisymmetric *B* field and is not excited, so that the transmission between $\lambda = 1.4\ \mu$m and $\lambda = 1.62\ \mu$m corresponds uniquely to the second band.

design parameters $m_1 = 1$, $m_2 = 4$, $\lambda_0 = 1.52\ \mu$m, which results in $a = 0.483\ \mu$m and $d = 1.3141\ \mu$m. Three cascaded layers are sufficient to achieve optimum coupling, but this optimum is only 70% at 1.52 $\mu$m due to large out-of-plane scattering losses (Fig. 10). The insertion efficiency at the non-mode-matched interface is calculated to be $8\% \pm 2\%$ and the peak insertion efficiency with the mode-matched interface is calculated to be 58% at 1.54 $\mu$m.

We simulate by FDTD the transmission through a PPC of 31 rows. We compute both the case of a PPC with two mode-matched interfaces and the case of a non-mode-matched PPC. We launch $|\psi_0\rangle$ and let it propagate through the structure. The transmission spectrum through the PPC (Fig. 11) results from two interfaces (unpatterned slab to PPC and PPC to unpatterned slab) as well as Fabry-Perot resonances between interfaces, losses inside the PPC for modes above the light line as well as near zero transmission inside the band gap. Both the total transmission through the PPC and the fraction of the transmitted power contained in $|\psi_0\rangle$ are shown. We attribute oscillations in the transmission spectrum to Fabry-Perot resonances between the interfaces.

In the case without any mode matching the transmission suddenly increases at the onset of the fourth band because Bloch modes of the fourth band essentially correspond to $|\psi_0\rangle$, as explained in Sec. III. The total transmission through the mode-matched PPC is enhanced in the frequency domain of the second band. The third band does not play any role because it has the opposite symmetry. Also the ratio between the fraction of the transmitted power contained in $|\psi_0\rangle$ and the total transmitted power is an order of magnitude higher in the mode-matched case: 81.45% versus 8.6% in the non-mode-matched case, at their respective peak transmission (at 1.55 $\mu$m and 1.57 $\mu$m).

The two interfaces of the PPC have a completely different transmission characteristic: In the case of the non-mode-matched PPC there is almost total reflection at the first interface (8% transmission), but high transmission at the second because the Bloch mode is free to diffract in all diffraction orders. Thus the insertion efficiency of the first interface is of the order of the total transmission. In the case of the mode-matched PPC the out-of-plane scattering losses due to the three layer MLG occur at both interfaces, so that the insertion efficiency is expected to be of the order of the square root of the total transmission. This can be formulated quantitatively: The insertion efficiency from the slab mode $|\psi_0\rangle$ into the PPC at the first interface is the same as the transmission efficiency from the PPC into $|\psi_0\rangle$ at the second interface (reciprocity principle). Hence, the insertion efficiency can be calculated as the square root of the fraction of the power transmitted in the zeroth order. This way the insertion efficiency is confirmed to be $8\% \pm 2\%$ for the non-mode-matched interface and is estimated to be 50% for the mode-matched interface at 1.55 $\mu$m, the wavelength of maximum transmission (the discrepancy from the previous, more rigorous calculation is easily taken into account by the Fabry-Perot effect).

The total power transmission through the PPC would be optimized by putting a mode matching interface only at the first interface. However, for integrated optics applications it will usually be necessary to mode match both interfaces, since it is the transmission into a particular slab mode that will matter if the PPC is interfaced with single mode optics. Even if the output field is collected by a multimode waveguide, the higher diffraction orders are likely to be outside the angle of total internal reflection of the waveguide ($\theta \simeq 56°$, where $\theta$ is the diffraction angle).

In the case of the non-mode-matched PPC the total trans-

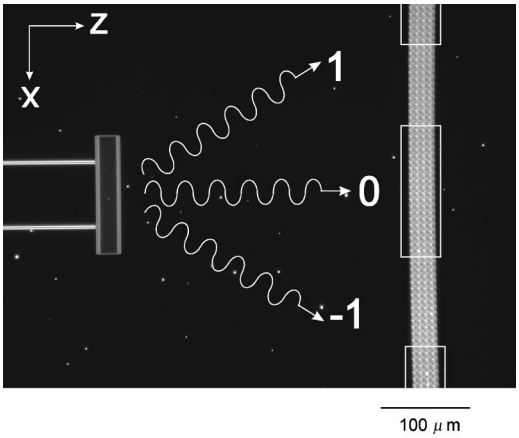


FIG. 12. Device imaged with a dark field microscope. On the left, a waveguide is connected to a mode-matched PPC. An amorphous crystal is placed to the right. Diffraction orders are numbered and represented by arrows. The white boxes show the regions imaged by the IR camera (Fig. 14).

mitted power at the second interface is a good estimate of the power incoming onto the second interface, so that the insertion efficiency can also be evaluated by the ratio between the transmitted power contained in $|\psi_0\rangle$ and the total transmitted power. Indeed this ratio is calculated to be 8.6% and is in accordance with the insertion efficiency calculated previously. However, this is not a good estimate in the case of the mode-matched PPC because there are significant out-of-plane scattering losses. But in this case the ratio between the transmitted power contained in $|\psi_0\rangle$ and the total transmitted power can serve to estimate the mode overlap, i.e., the insertion efficiency with the internal losses of the MLG normalized out (81%). This number is very close to the total insertion efficiency obtained with the MLG composed of 40 nm holes, which is not limited by out-of-plane scattering (84%).

## VIII. EXPERIMENTAL DEMONSTRATION

We experimentally image the diffraction pattern of a Bloch mode after it propagates through the PPC and crosses the interface to the unpatterned slab. We compare the case of a non-mode-matched PPC and of a mode-matched PPC. In the latter case a three layer MLG with holes of radius $r = 0.15\ \mu$m is added to the interface. In the absence of a mode matching interface the Bloch mode gives rise to higher diffraction orders that are the signature of the higher-order Fourier components in the Bloch mode structure. When the MLG is added to the PPC the higher diffraction orders are suppressed. Because of reciprocity, this is expected when the mode matching efficiency is high.

Devices were fabricated by *e*-beam lithography (Leica EBPG 5000+ at 100 kV) on silicon on insulator (SOI) samples with a 205 nm silicon membrane. Prior to lithography an 80 nm sputtered $SiO_2$ film was deposited. After the *e*-beam lithography the pattern was transferred from the polymethyl methacrylate into the silicon dioxide with a $CHF_3$ reactive ion etch and from the silicon dioxide into the

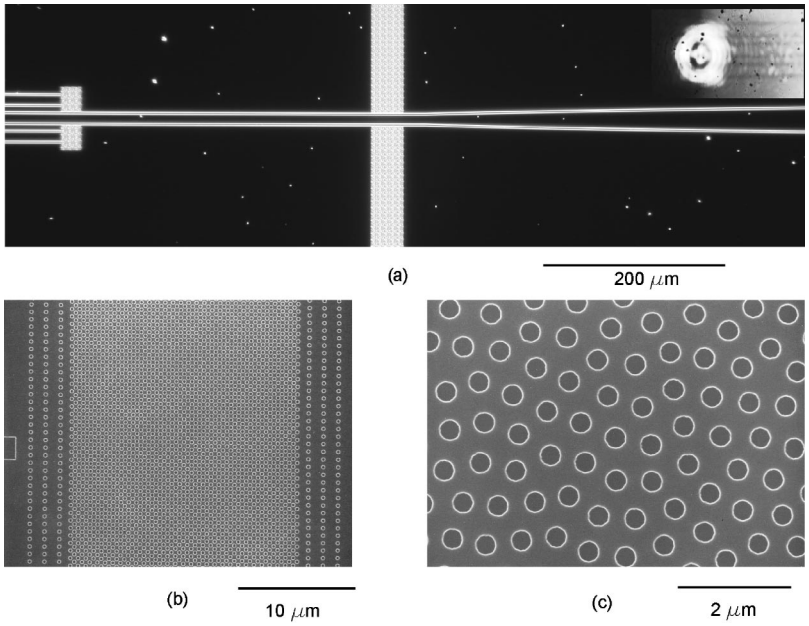


FIG. 13. (a) Dark field microscope image of the waveguide region before the photonic crystal. On the left three waveguides are seen. The center one is tapered out and couples into the photonic crystal (Fig. 12). In the center of the image the white bar corresponds to an amorphous crystal that extracts stray light coupled from free space into the slab (outside of the waveguide). This makes sure that the light imaged in the region of the PPC is coupled from the center waveguide. The upper and lower waveguides on the left of the picture are used as fiducials to optimize coupling from free space: In order to center the position of the spot from the focusing lens, we aimed to have an equal amount of light extracted by the amorphous crystals at the terminations of the two outer waveguides. The inset is a picture taken with the IR camera. The spot from the focusing lens can be seen as well as the three waveguides. (b) is an SEM picture of the mode-matched PPC and (c) is an SEM view of the amorphous crystal.

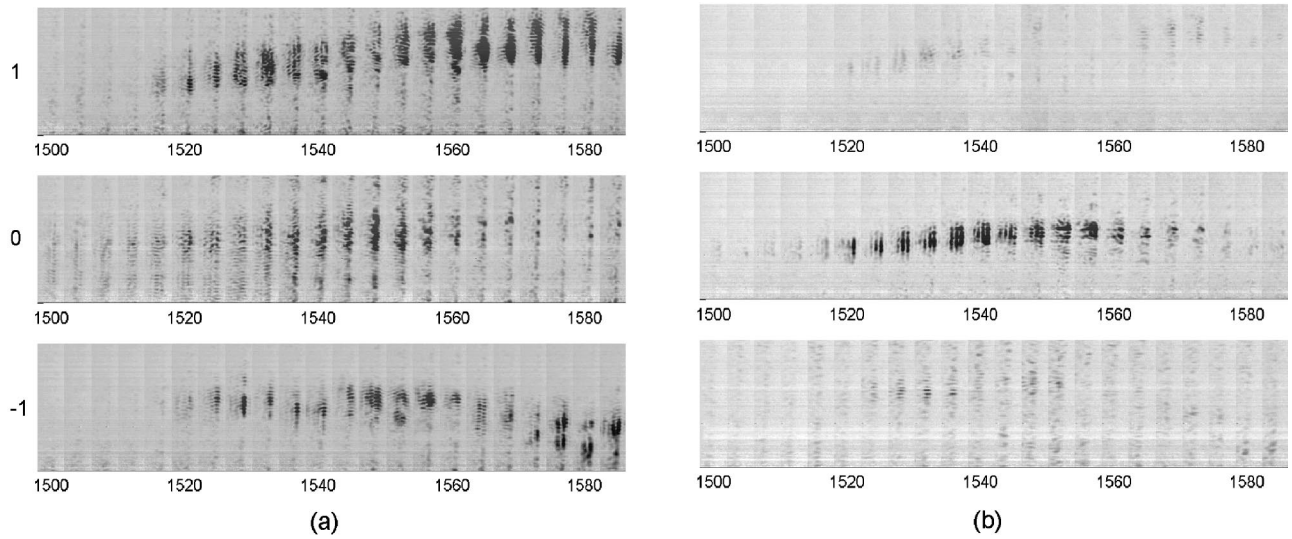


FIG. 14. (a) Experimental results for the non-mode-matched PPC. The amorphous crystal is imaged with an IR camera for each subsequent wavelength. The intensities of all diffraction orders are shown. (b) Experimental results for the mode-matched PPC. The diffraction orders 1 and $-1$ are suppressed. In (a) and (b), the color scaling is the same for the three diffraction orders. The settings of the infrarred camera were the same and the spots were imaged on the same region of the $In_xGa_{1-x}As$ diode array.

silicon with a Cl inductively coupled plasma reactive ion etch. Finally, a 1 $\mu$m sputtered $SiO_2$ film was deposited on top as a cladding layer.

In order to compensate for small variations in refractive indeces and film thickness, we fabricated several samples corresponding to variations in $\lambda_0$, the target wavelength of the MLG [varying $\lambda_0$ is equivalent to varying $n$ in Eqs. (3) and (4)]. The best suppression of the diffraction orders 1 and $-1$ at the output of the mode-matched PPC was achieved for $\lambda_0 = 1.565$ $\mu$m. The lattice constant of the PPC is dependant on $\lambda_0$ as indicated in Sec. III and varies slightly throughout the span. For $\lambda_0 = 1.565$ $\mu$m, $a = 0.470$ $\mu$m, and $d = 1.277$ $\mu$m.

Polarized light is butt coupled into a 10 $\mu$m wide waveguide with a 100$\times$ long working distance lens. The waveguide is expanded with a parabolic taper [22] to the final width $W = 70$ $\mu$m [$W(y)^2 = (2\lambda_0/n)y + W_0^2$, where $\lambda_0 = 1.52$ $\mu$m and $W_0 = 10$ $\mu$m, Fig. 13(a)]. A PPC with 59 rows of holes [Fig. 13(b)], with bare or mode-matched interfaces, is placed at the end of the waveguide. The field then diffracts into the unpatterned slab. 325 $\mu$m away from the PPC an amorphous crystal [Figs. 12 and 13(c)] vertically extracts light that is subsequently imaged by an IR camera (Indigo systems, Merlin InGaAs NIR). The crystal is amorphous so that it has an isotropic in plane behavior [23,24], i.e., light guided by the slab is vertically extracted [25] independently of its angle of incidence [26].

Figure 14 shows the diffraction patterns as imaged by the IR camera. The diffraction orders $-1$, 0, and 1 have different propagation directions and separate into three separate beams. Those beams then impact on the amorphous crystal and get extracted out of the slab, thus three bright spots appear on the amorphous crystal. Those spots are imaged by the IR camera and are shown in Fig. 14. The light is generated by a tunable laser and this measurement is repeated for free space wavelengths ranging from 1.5 $\mu$m to 1.58 $\mu$m. The white boxes in Fig. 12 correspond to the imaged regions shown in Fig. 14. It can be seen that the $-1$ and 1 diffraction orders are suppressed in Fig. 14(b). The pass band of the mode-matched device is 40–50 nm and corresponds to the pass band calculated in Sec. VII.

## IX. CONCLUSION

We have shown that a diffraction grating composed of multiple rows of holes can be designed to mode match between a planar photonic crystal and an unpatterned slab. We achieved 84% insertion efficiency with a multilayered grating composed of 19 layers of holes with a radius of 40 nm, compared to 9% without mode matching. It is possible to design more compact structures with bigger holes at the cost of significant out-of-plane scattering losses and a corresponding decrease in insertion efficiency. In particular, 58% insertion was achieved with a multilayered grating composed of three rows of holes with a radius 0.15 $\mu$m. Despite their reduced insertion efficiency, these more compact structures are of interest because they enable coupling into a planar photonic crystal of beams with a smaller width.

## ACKNOWLEDGMENTS

The authors would like to thank Maxime Rattier for useful discussions. The authors wish to acknowledge generous support from DARPA under Contract No. N-00421-02-D3223, and the AFOSR under Contract No. F49620-03-1-0418.

[1] E. Yablonovitch, Phys. Rev. Lett. **58**, 2059 (1987).
[2] T.F. Krauss, R.M. De La Rue, and S. Brand, Nature (London) **383**, 699 (1996).
[3] S.-Y. Lin, V.M. Hietala, L. Wang, and E.D. Jones, Opt. Lett. **21**, 1771 (1996).
[4] B. Gralak, S. Enoch, and G. Tayeb, J. Opt. Soc. Am. A **17**, 1012 (2000).
[5] M. Notomi, Phys. Rev. B **62**, 10 696 (2000).
[6] C. Luo, S.G. Johnson, J.D. Joannopoulos, and J.B. Pendry, Phys. Rev. B **65**, 201104 (2002).
[7] H. Kosaka, T. Kawashima, A. Tomita, M. Notomi, T. Tamamura, T. Sato, and S. Kawakami, Phys. Rev. B **58**, R10096 (1998).
[8] H. Kosaka, T. Kawashima, A. Tomita, M. Notomi, T. Tamamura, T. Sato, and S. Kawakami, Appl. Phys. Lett. **74**, 1370 (1999).
[9] L.J. Wu, M. Mazilu, T. Karle, and T.F. Krauss, IEEE J. Quantum Electron. **38**, 915 (2002).
[10] H. Kosaka, T. Kawashima, A. Tomita, M. Notomi, T. Tamamura, T. Sato, and S. Kawakami, Appl. Phys. Lett. **74**, 1212 (1999).
[11] D.N. Chigrin, S. Enoch, C.M. Sotomayor Torres, and G. Tayeb, Opt. Express **11**, 1203 (2003).
[12] J. Witzens and A. Scherer, J. Opt. Soc. Am. A **20**, 935 (2003).
[13] L. Wu, M. Mazilu and T.F. Krauss, J. Lightwave Technol. **21**, 561 (2003).
[14] C. Chen, A. Sharkawy, D.M. Pustai, S. Shi, and D.W. Prather, Opt. Express **11**, 3153 (2003).
[15] X. Yu and S. Fan, Appl. Phys. Lett. **83**, 3251 (2003).
[16] T. Baba and D. Ohsaki, Jpn. J. Appl. Phys., Part 1 **40**, 5920 (2001).
[17] J. D. Joannopoulos, R. D. Meade, and J. N. Winn, *Photonic Crystals: Molding the Flow of Light* (Princeton University Press, Princeton, 1995).
[18] A. Yariv, *Optical Electronics in Modern Communications* (Oxford University Press, New York, 1991).
[19] C. F. Bohren and D. R. Huffman, *Absorption and Scattering of Light by Small Particles* (Wiley, New York, 1983).
[20] A. W. Snyder and J. D. Love, *Optical Waveguide Theory* (Chapman and Hall, Australian National University, Canberra, 1983).
[21] J. Witzens, T. Baehr-Jones, M. Hochberg, M. Lončar, and A. Scherer, J. Opt. Soc. Am. A **20**, 1963 (2003).
[22] W.K. Burns, A.F. Milton, and A.B. Lee, Appl. Phys. Lett. **30**, 28 (1977).
[23] Y.S. Chan, C.T. Chan, and Z.Y. Liu, Phys. Rev. Lett. **80**, 956 (1998).
[24] S. David, A. Chelnokov, and J.-M. Lourtioz, IEEE J. Quantum Electron. **37**, 1427 (2001).
[25] M. Boroditsky, T.F. Krauss, R. Coccioli, R. Vrijen, R. Bhat, and E. Yablonovitch, Appl. Phys. Lett. **75**, 1036 (1999).
[26] M. Rattier, H. Benisty, E. Schwoob, C. Weisbuch, T.F. Krauss, C.J.M. Smith, R. Houdre, and U. Oesterle, Appl. Phys. Lett. **83**, 1283 (2003).